Applied Catalysis A, General xxx (xxxx) 118833

Contents lists available at ScienceDirect

Applied Catalysis A, General

journal homepage: www.elsevier.com/locate/apcata

The effect of Ni particle size and carbon support on catalytic activity for glucose hydrogenation reaction

Yang Fu [a], François Devred [a], Pierre Eloy [b], Tommy Haynes [a], Michael L. Singleton [a], Sophie Hermans [a]

[a] IMCN Institute, MOST Division, UCLouvain, 1 Place Louis Pasteur, B-1348 Louvain-la-Neuve, Belgium
[b] IMCN Institute, BSMA Division, UCLouvain, 1 Place Louis Pasteur, B-1348 Louvain-la-Neuve, Belgium

ARTICLE INFO

Keywords:
Glucose, hydrogenation
Non-noble metal
Size effect, carbon black

ABSTRACT

Ni nanoparticles supported on carbon black (Ni/CB) with Ni particle sizes 6.9–23.5 nm were found to exhibit a size effect, with a significant impact on catalytic performance in the glucose hydrogenation reaction. A series of Ni nanoparticles with different sizes, as determined by statistical analysis of TEM images, were obtained by varying the synthesis temperature using a sol-gel method. The highest glucose conversion and sorbitol production in glucose hydrogenation was possible with Ni/CB catalysts with Ni particles size around 17 nm obtained at 550 °C. Similarly, graphene nanoplatelets (GNP) supported Ni with different particle sizes synthesized under different temperature conditions have an identical behaviour, that is, GNP-550 exhibits the highest catalytic performance. Therefore, it can be concluded that size effect appeared when the particle size is above 10 nm, which provides a reference for the design of subsequent catalysts for liquid phase hydrogenation reactions pertinent to biomass conversion.

1. Introduction

Sorbitol as a sweetener, moisturizer, texturizer and softener is largely used in the food industry, for medical applications as well as cosmetics. Its global market size was valued at USD 1244.5 million in 2018 and is predicted to rise to 1928.3 million by the end of 2026, showing a compound annual growth rate (CAGR) of 5.54 % in the forecast period 2019–2026 [1]. Sorbitol is produced mostly by glucose catalytic hydrogenation. Metal catalysts applied in the process have been investigated among Ni, Pt, Co, Ru metals and their multicomponent structures with promoters like P, B, Al, Fe [2–17]. Among these catalysts, Raney type Ni was the first to be applied as early as in 1912 [18]. For Raney nickel catalysts, a large amount of metal leaching during the reaction is an inevitable issue. It can be diminished by reducing the amount of Ni used and stabilizing small metal particles by supports like SiO_2, C, zeolite [6,12]. On the contrary, noble metals do not have this leaching problem and usually possess absolute advantages in their catalytic activity compared to base metals. For example, the conversion of glucose and selectivity to sorbitol with a Ru catalyst presenting a 0.6 wt % metal loading were comparable to a Ni catalyst with a 66.78 wt % metal loading and no leaching was detected after 1155 h time on stream [19]. Besides Ru catalysts, other noble metals like Pt also have a higher activity than Ni catalysts but not as good as Ru catalyst [13]. Ruthenium and Nickel catalysts are both used to produce sorbitol from glucose solutions in the industry right now. In comparing further these two catalysts, an obvious cost issue arises, as Ru metal is more expensive than Ni metal by a factor 1000. For this reason, there has been a demand for the modification of low-cost Ni catalysts to enhance their catalytic performance as potential alternatives of Ru catalysts.

The modification of supported metal catalysts can be achieved by altering the support and tuning the morphology of the metal particles such as size and shape [20–23]. Due to the fact that electronic structures of metal particles change along with the size ranges (nanoparticles, cluster, single atom), extensive research has been done by many authors focusing on the size effect among single atoms, clusters and small nanoparticles. For example, the turnover frequencies for CO oxidation per surface gold atom of Au catalysts supported on TiO_2, α-Fe_2O_3, and Co_3O_4 were found independent of the supports used but increase sharply with a decrease in diameter of gold particles below 4 nm [24]. And Pd particles supported by carbon black with a size centred on 7 nm present an optimal activity in the glucose oxidation reaction [25]. It was also demonstrated that most active Pd/h-BN catalysts must have a particle size distribution between 3 and 15 nm for lactose oxidation [26]. Charge transfer between the metal particle and support was demonstrated to account for the size effect in the case of a well-defined platinum/ceria catalyst by combing synchrotron radiation photoelectron spectroscopy, scanning tunnelling microscopy and density functional calculations, and Pt with a size around 1–1.5 nm was calculated to have a maximum charge transfer [27]. Thus, most of the size effects

https://doi.org/10.1016/j.apcata.2022.118833
Received 16 May 2022; Received in revised form 28 July 2022; Accepted 15 August 2022
0926-860/

were found in nanoparticles smaller than 10 nm, and the catalytic properties remain unchanged as the nanoparticles increase in size [28]. However, this size effect varies with the reaction considered as well as with the used metal itself. Therefore, it is meaningful to investigate the size effect of Ni nanoparticles larger than 10 nm in glucose hydrogenation. These can be even considered as model structures for local domains in Raney Ni.

Here, we prepared carbon black (CB) and graphene nanoplatelets (GNP) supported Ni catalysts (Ni/CB and Ni/GNP) by sol-gel method, and Ni particles with different sizes were obtained by controlling the temperature during the synthesis. In situ XRD was applied to probe the growth of Ni particles and ex situ XRD was used to analyse the catalysts obtained after each synthesis. The obtained catalysts were used to catalyse the glucose hydrogenation reaction in the liquid phase under high pressure. The conversion of glucose, the yield of sorbitol and other by-products were analysed to reveal the relation between the Ni particle size (over 10 nm) on CB and GNP support and their catalytic performance. N_2 sorption isotherms, XPS, TGA, ICP-AES and H_2-TPD and TEM were also applied for a comprehensive analysis of catalysts properties.

2. Experimental

2.1. Chemicals and materials

Carbon black [250 G type, IMERYS GRAPHITE & CARBON], graphene nanoplatelets (M15, Sigma-Aldrich), Nickel (II) nitrate hexahydrate [Ni $(NO_3)_2$0.6 H_2O, 99.999 %, Sigma-Aldrich], citric acid [$C_6H_8O_7$, 99.5 %, Alfa Aesar], and ethanol [C_2H_5OH, 100 %, Merck] were used as received.

2.2. Catalysts preparation

2.2.1. Ni nanoparticles supported on carbon black (Ni/CB)

Pechini-type sol-gel method was used for the preparation of supported catalysts [29]. Typically, 1.6 g of citric acid, 0.4 g of CB, 1.7 mmol of the Ni $(NO_3)_2$0.6 H_2O (495.2 mg of Ni $(NO_3)_2$0.6 H_2O) and a stirring bar were introduced into a round-bottom flask, respectively. After 16 mL of ethanol was added, the mixture was stirred for 10 min, then sonicated for another 20 min at the power level of 4 (VWR ultrasound cleaner USC 1200-THD). After the mixture was heated at 90 °C for 3 h under reflux, it was transferred into a 33 mL ceramic boat and then dried at 30 °C under vacuum until a gel formed. The obtained gel was then introduced into a tubular furnace and heated to 300 °C for 2 h under H_2/ Ar atmosphere. The recovered powder was labelled as CB-300, which was treated as a seed for further particles growth through heat treatment. To do so, CB-300 was reintroduced into the tubular furnace and heated to a set temperature for 1 h under Ar/H_2 atmosphere. Afterwards, the final catalyst was obtained and named according to the temperature of heat treatment (CB-xxx). In that way, CB-400, CB-500, CB-550, CB-600 and CB-650 catalysts were prepared at 400, 500, 550, 600 and 650 °C, respectively. Those catalysts were used without further precautions.

2.2.2. Ni nanoparticles supported by GNP

Ni nanoparticle supported by GNP catalysts were synthesized using the same method as mentioned above by replacement of the carbon support. Consequently, GNP-350, GNP-450, GNP-550 and GNP-650 were obtained through the heat treatment of GNP-300 at 350, 450, 550 and 650 °C.

2.3. Catalyst characterization

Transmission electron microscopy (TEM) images TEM images were acquired on a LEO 922 Omega Energy Filter Transmission Electron Microscope under an operating voltage of 120 kV. For the sample preparation, Ethanol was used to suspend the samples. After ultrasonic treatment, few drops of the suspension were deposited on a holey carbon film supported on a copper grid (Holey Carbon Film 300 Mesh Cu), which was dried before introduction in the microscope for imaging.

X-ray photoelectron spectroscopy (XPS) analyses were performed with an SSI-X-probe (SSX 100/206) photoelectron spectrometer from Surface Science Instruments (USA) at room temperature and monochromatized microfocus Al X-rays (1486.6 eV) were used as a source. Samples were placed on the round metal stage sample holders using double face adhesive tape and then the sample holders were fixed on an insulating ceramic carousel (Macor®, Switzerland). A nickel grid above the carousel and a flood gun set at 8 eV were applied to eliminate the charging effect of the samples during analysis. Data analysis was executed using CasaXPS software, and the peaks were decomposed by Gaussian/Lorentzian product formula GL (15) after a Shirley-type background was subtracted. All the binding energies were calibrated according to the C-(C, H) component of the C 1 s peak fixed at 284.8 eV.

X-ray diffraction (XRD) analysis were performed using a Bruker D8 advanced diffractometer (Bragg-Brentano geometry) equipped with a LInkeye XE-T detector. The powder sample was spilled on a silicon crystal sample holder with a thin layer of NIVEA cream as an adhesive. The X-ray source (Cu kα1,2, $\lambda = 0.15418$ nm) operates at 1200 W (30 mA, 40 kV). Analysis were made within a 2θ range from 5° to 80° using a step size 0 f 0.015° and 0.15 s per step. For in-situ experiments, a Paar Instrument XRK 900 chamber was used to control the reducing atmosphere (30 mL/min of 5 % H_2 in argon) and the temperature (from 300 C to 700 C). Thermal expansion of the chamber is adjusted by correcting the height of the sample at each temperature. Eva software (Bruker) and the PDF-2 database were used for data treatment.

For thermogravimetric analyses (TGA), 5–10 mg samples were placed in alumina containers and introduced in a Mettler Toledo TGA/SDTA 851e instrument. Thermograms were recorded up to 900 ºC using a 10 °C/min heating rate under a 99.999 % N_2 flux.

Ni weight percentage in the bulk CB/GNP supported catalysts were obtained using ICP-AES Varian 720ES by analytical and chemical consultancy services from MEDAC LTD (UK). The samples were digested with 5 mL of nitric acid and 1 mL of hydrogen peroxide, then the solutions were made up to a volume with 18.2 Mohm water and analysed. The amount of Ni leaching after the catalytic tests was analysed within the products solutions by Perkin Elmer 3100 Atomic Absorption Spectrometer (AAS) after filtering out the solid catalyst.

Temperature-programmed desorption (TPD) experiments were performed on a Catlab equipment from Hiden (UK). Typically, a sample of ca. 60 mg was treated under a 30 mL/min flow of 5 % H_2/Ar at 300 °C for 1 h, and subsequently cooled down at 50 °C. The same reductive atmosphere was maintained for 1 h. After that, the sample was purged with pure Ar (30 mL/min) for 1 h to eliminate the physical absorbed H_2 and H_2-TPD profiles were recorded in flowing Ar in the temperature range 50 – 800 °C with a heating rate of 10 °C/min.

The specific surface area of the catalysts was determined using a Micromeritics ASAP 2020 analyser by nitrogen adsorption-desorption isotherms at 77 K. Around 200 mg of sample was first degassed for 2 h under 0.133 Pa pressure at 473 K with a heating rate of 10 K/min. The specific surface areas were calculated based on the well-established Brunauer-Emmett-Teller (BET) equation by analysis of the isotherms.

2.4. Hydrogenation of D-glucose

Aqueous glucose hydrogenation was carried out in a 300 mL stainless-steel high-pressure reactor (Parr Instrument Company). For a typical reaction, 0.5 g of glucose, 0.06 g of catalyst and 100 mL Milli-Q water was first introduced into the reactor. After the reactor was fasten into its mantle, N_2 was purged for 5 min to remove the air in the reactor. Then the reactor was heated until 140 °C. H_2 was filled at a pressure of 30 bar and motor was switched on at a stirring rate of 1700 rpm

(which was sufficient to eliminate external mass-transport limitations), at which point the reaction started. After 2 h reaction, the reaction was immediately stopped by simultaneously releasing the hydrogen pressure and cooling down to room temperature with circulating water. Reaction slurry was filtrated on PVDF membrane (0.2 μm), and the recovered solid was washed with Milli-Q water and dried at room temperature overnight. This solid is the spent catalyst that will be used for recycling tests. The filtrate was systematically analysed to evaluate the glucose conversion, product yields and leaching of Ni. For a recycling test, the same reaction conditions were kept except that the catalyst was replaced by the spent catalyst.

For the analysis of products, the filtrate was analysed by HPLC. A refractive index 2414 detector and an HPX-87 C carbohydrate column were equipped into a Waters system HPLC. Milli-Q water was used as mobile phase at a flow rate of 0.5 cm^3 min^{-1}. The injected volume is 25 μl and the column temperature was set at 358 K. Standard alpha-D (+)-glucose ($C_6H_{12}O_6$, ≥ 99 %, Acros), D-sorbitol ($C_6H_{14}O_6$, ≥ 99.5 %, Sigma), D-(-)-fructose ($C_6H_{12}O_6$, ≥ 99, Sigma), D-mannitol ($C_6H_{14}O_6$, ≥ 98 %, Sigma-aldrich) and D-(+)-mannose ($C_6H_{12}O_6$, ≥ 99 %, Sigma), with a known gradient concentration were first analysed by HPLC separately to determine their retention times and signal intensity – concentration relation, which were used as references to identify and quantify the products of glucose hydrogenation. The glucose conversion, sorbitol selectivity, product percentage yield and sorbitol productivity were calculated according to Eqs. (1–4):

$$Conversion\ (\%) = \frac{moles\ of\ glucose\ (t = 0) - moles\ of\ glucose\ (t}{}$$

$$Selectivity\ (\%) = \frac{moles\ of\ sorbitol}{moles\ of\ glucose\ (t = 0) - n}$$

$$\text{Yield}\ (\%) = \frac{\text{moles of product (t = i)}}{\text{moles of glucose (t = 0)}} \times 100 \quad (3)$$

$$Sorbitol\ \ productivity = \frac{mass_{sorbitol}}{time * \ mass_{catalyst}} \quad (4)$$

3. Results and discussion

3.1. Characterization of Ni/CB catalysts

During the synthesis of our starting carbon-supported Ni catalyst, a gel is formed after the ethanol was evaporated for 2 h under vacuum, which allows a nice distribution of the metal precursors. Thanks to coalescence and Ostwald ripening, it allows us to control the Ni particle size simply by altering subsequent heat treatment temperature and duration under a reductive atmosphere [25,30–34]. Ni nanoparticle growth with temperature was monitored by in situ p-XRD, diffraction patterns of which are shown in Fig. 1a and Fig. S1. The starting CB-300 gave an almost flat curve at the bottom of the diffraction patterns, which is due to the Ni grain size being less than 5 nm and possibly the amorphous texture of remaining reagents [35]. When the temperature increased to 350 °C, a diffraction hump at 2θ ≈ 44° becomes visible, which corresponds to the diffraction by Ni face centered cubic (fcc) (111) planes (JCPDS-ICDD card No.40–0850). As the temperature continued to rise, this hump became sharper and sharper and a diffraction peak at 2θ ≈ 51° assigned to the (200) crystal plane of fcc nickel, appeared. This latter turns to be more visible after the temperature reached 450 °C. Since the grain increased with the temperature increment, the full width at half maximum (FWHM) decreased, inducing a shaper peak after a higher temperature treatment. Due to the thermal expansion of the crystalline unit cells, the diffraction peaks shifted to the left as the temperature increased. Once the final sample was cooled down to 35 °C (yellow curve on the top in Fig. 1a), the peaks restored to their original positions but the values of FWHMs remained similar to that of 700 °C. Based on the diffraction patterns collected at different temperatures, we calculated the grain sizes of Ni particles from the FWHMs of (111) diffraction peaks using Scherrer equation, and the results are illustrated in Fig. S2. The Ni grain grows from ~3.8 nm at

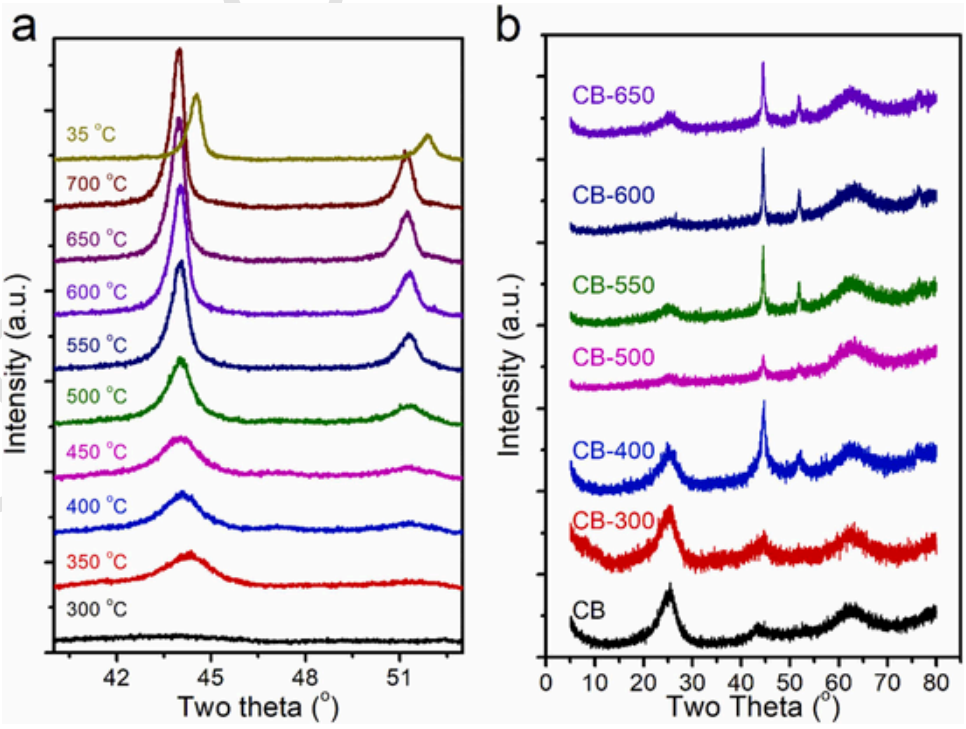

Fig. 1. a) In situ XRD patterns of CB-300 recorded every 50 °C from 300 °C to 700 °C. b) ex situ XRD patterns of prepared Ni nanoparticles supported by CB at the corresponding temperatures of heat treatment marked in the names of the samples. The XRD pattern of pure CB is shown at the bottom as a blank reference.

300 °C to ~13.4 nm at 700 °C, and in the temperature ranges of 300–450 °C and 600–700 °C, the grain sizes changed the least. Given this result, temperatures at 400, 500, 550, 600 and 650 °C were chosen to prepare the diverse sizes of Ni nanoparticles supported on CB. The XRD patterns of obtained catalysts are shown in Fig. 1b. The XRD pattern of pure CB support (black curve) is given as a reference. One broad peak at 2θ = 25.4° is attributed to the (002) plane of graphite (JCPDS-ICDD card No.41–1487), which reveals the disordered graphitic nature of CB. For the catalysts, the peak at 2θ = 44.7° attributable to the Ni fcc (111) plane started appearing in CB-400 and grow with the temperature increase, and the same happened with the peak at 2θ = 51.9°. The Ni grain sizes of all the prepared catalysts were also calculated with the Scherrer equation based on FWHMs of the Ni (111) diffraction peaks and the results are displayed in Table 1. It was observed that the grain sizes exhibit a distinct variation in different catalysts, with a size growth with temperature, except for CB-550, CB-600 and CB-650, which is consistent with the above in situ XRD outcome. Smaller sizes were obtained in the in situ XRD experiments than with ex situ XRD, due to the heat duration in the former that is shorter than the latter (1 h) where it allows the particles to grow more with time. It should be noted that the intensities of the diffraction peaks alter from sample to sample in Fig. 1b, which is due to the different quantities of samples used for measurements. However, the FWHMs of peaks are not affected by peak intensities variations due to this effect.

Table 1
Nickel particle sizes in Ni/CB catalysts calculated from XRD patterns and TEM images; Ni weight percentages in the prepared catalysts determined by ICP-AES.

Entry	Size / nm		Ni wt%
	XRD	TEM	
CB-300	4.9	–	11.8
CB-400	8.3	6.9 ± 1.3	16.5
CB-500	13.4	12.6 ± 3.8	18.3
CB-550	19.1	17.1 ± 6.7	20.7
CB-600	21.1	22.0 ± 10.0	21.2
CB-650	20.4	23.5 ± 11.6	19.3

The particle morphology identified by TEM imaging and the related statistics histograms are illustrated in Fig. 2 and 3. Diverse Ni nanoparticle profiles were obtained along with different synthesis temperature conditions. The Ni particles synthesized at a temperature of 400 °C display a more homogeneous size range than others, and as the temperature increased, more and more particles with larger sizes appeared. To further illustrate the size distribution in the different samples, 100 particles in the TEM images of each sample were selected for statistical analysis. Statistical values of average particle sizes are displayed in

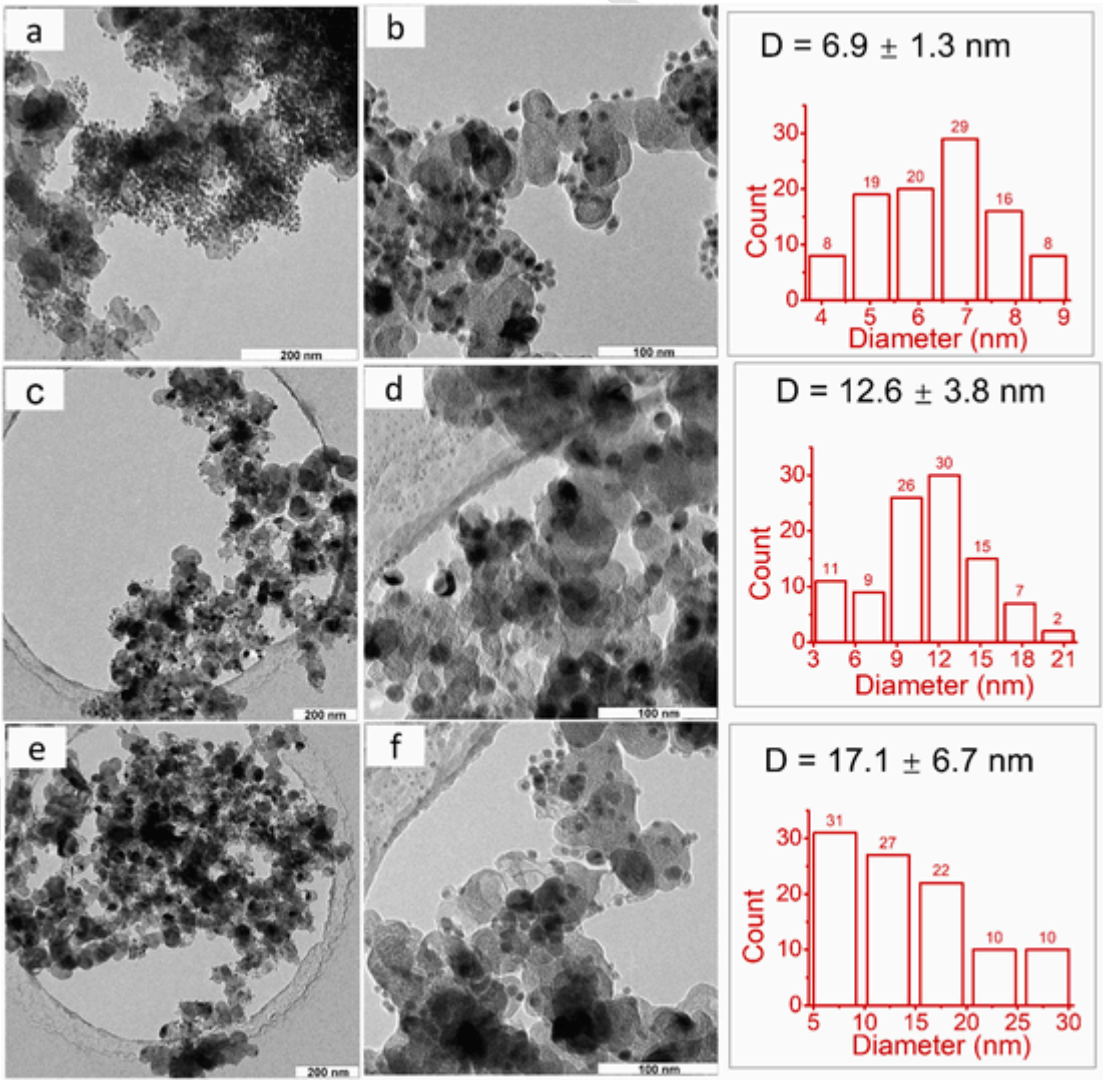

Fig. 2. TEM images of CB-400 (a, b), CB-500 (c, d), CB-550 (e, f) samples. The corresponding statistical histograms of particle sizes are shown at the right of each two images and the average diameter (D) is written in the histograms.

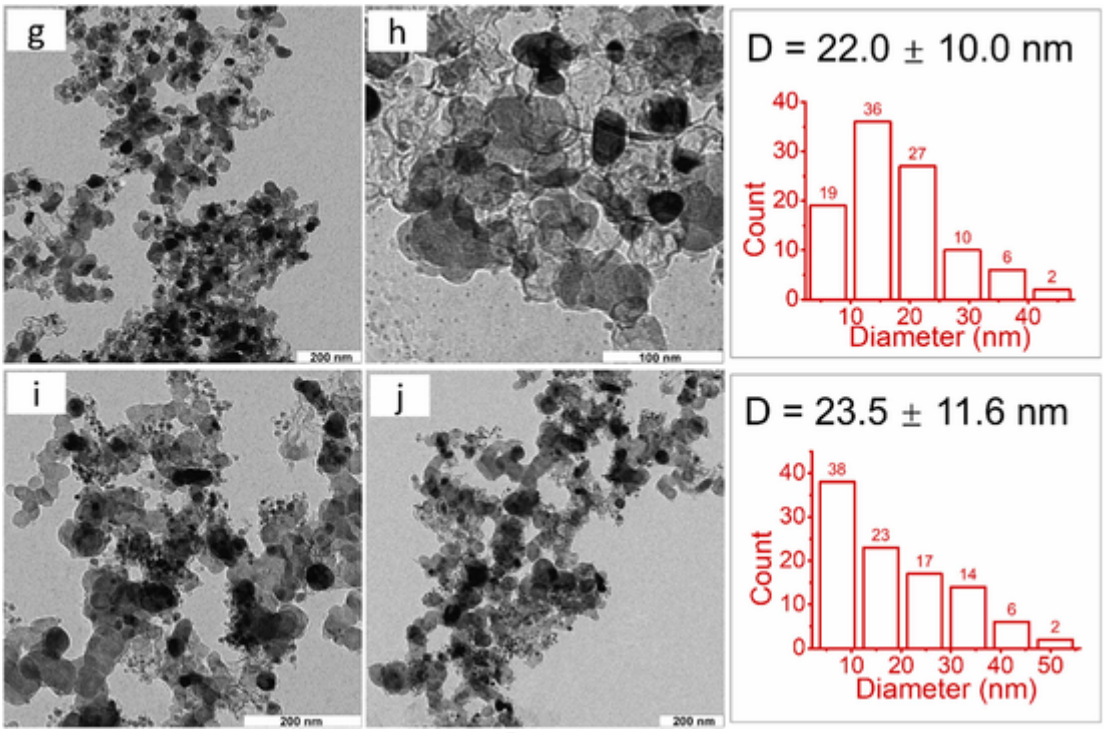

Fig. 3. TEM images of CB-600 (g, h) and CB-650 (i, j) samples. The corresponding statistical histograms of particle sizes are shown at the right of each two images and the average diameter (D) is written in the histograms.

Table 1. For the CB-400 catalyst, its average size is around 6.9 nm, and when the synthesis temperature increases, the size of the obtained particles increases accordingly, which is consistent with the XRD results. At the same time, higher temperature induces larger variation of particle size distribution, for which standard deviation increases from 1.3 nm at 400 °C to 11.6 nm at 650 °C. Besides, regardless of the temperature condition, there are always Ni particles around 7 nm present in all the samples, which is due to the fact that Ni particles were prepared by heat treatment of identical starting CB-300 material and that the heat-treatment was not prolonged.

The Ni metal loading of CB-series catalysts were analysed using ICP-AES and the results are also shown in Table 1. With the increase of synthesis temperature, the Ni content first increased from 11.8 wt% for CB-300–20.7% for CB-550, and then stayed a constant value around 20 % for CB-600 and CB-650. The lowest Ni loading for CB-300 is due to the incomplete decomposition and reduction of the reactants, which can be further reduced at high temperature, inducing a higher Ni loading for the next samples that have been further heated. The similar Ni loading for CB-550, CB-600 and CB-650 suggests that all the reactants were well decomposed leaving only Ni particles and CB support in the samples from a reduction temperature of 550 °C. This result can also be demonstrated by TGA analysis (Fig. 4). 28.5 % of weight loss in CB-300 when it was heated until 450 °C is observed, implying the gel texture formed by citric acid and the metal precursor that were remaining in CB-300 sample. There is less than 3.4 % of weight loss for other samples before 450 °C, and after 450 °C the trend of the curves is almost the same. It should be noted that the weight increases around 0.8 % before 450 °C can be attributed to the buoyancy effect on the sample holder. The gas density in the space where the sample holder is located decreases with the increase of temperature, and thus the buoyancy decreases, which manifests itself as an apparent weight gain. This effect being very small is only visible in the absence of any other mass loss/gain and by zooming in on the TGA curve as done here.

XPS analysis was applied to determine the surface chemical composition and metal oxidation states within the catalysts. Fig. 5 illustrates the high resolution XPS Ni $2p_{3/2}$ spectra of those obtained catalysts.

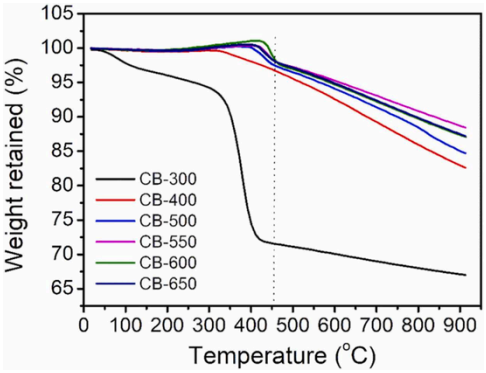

Fig. 4. TGA curves of CB-300 (black), CB-400 (red), CB-500 (blue), CB-550 (pink), CB-600 (green) and CB-650 (dark blue) recorded under N_2 atmosphere from 25 to 900 °C with a heat rate of 10 °C / min.

The peak with binding energy around 853 eV is ascribed to metallic Ni (Ni^0). The peaks (blue components) around 856 eV are assigned to oxidized Ni ($Ni^{\delta+}$), along with satellite peaks (pink components) [36]. The binding energy and contents of Ni^0 and $Ni^{\delta+}$ as well as elemental analysis result of the Ni/C ratio are listed in Table 2. In the CB-300 sample, there is no metallic Ni present, while in the other samples, more than half of the Ni state detected is Ni^0. The oxidized species in CB-300 come from the Ni precursors that do not get reduced spontaneously at such low temperature. As the temperature increases, Ni will get reduced but surface re-oxidation of Ni could occur during the handling and storage. Furthermore, the Ni^0 proportion in the catalysts increases with the treatment temperature, which is due to high temperatures facilitating the hydrogen diffusion and reduction of Ni precursor. This could help the catalyst to maintain the metallic surface from being oxidized when exposed to the air. A similar Ni/C atomic ratio was present on the surface of CB-400, CB-500, CB-550, CB-600 and CB-650 catalyst, as determined by XPS. For CB-300 catalyst, it has a Ni/C mass ratio of 6.17 %, higher than other catalysts, which means that CB-300 presents the high-

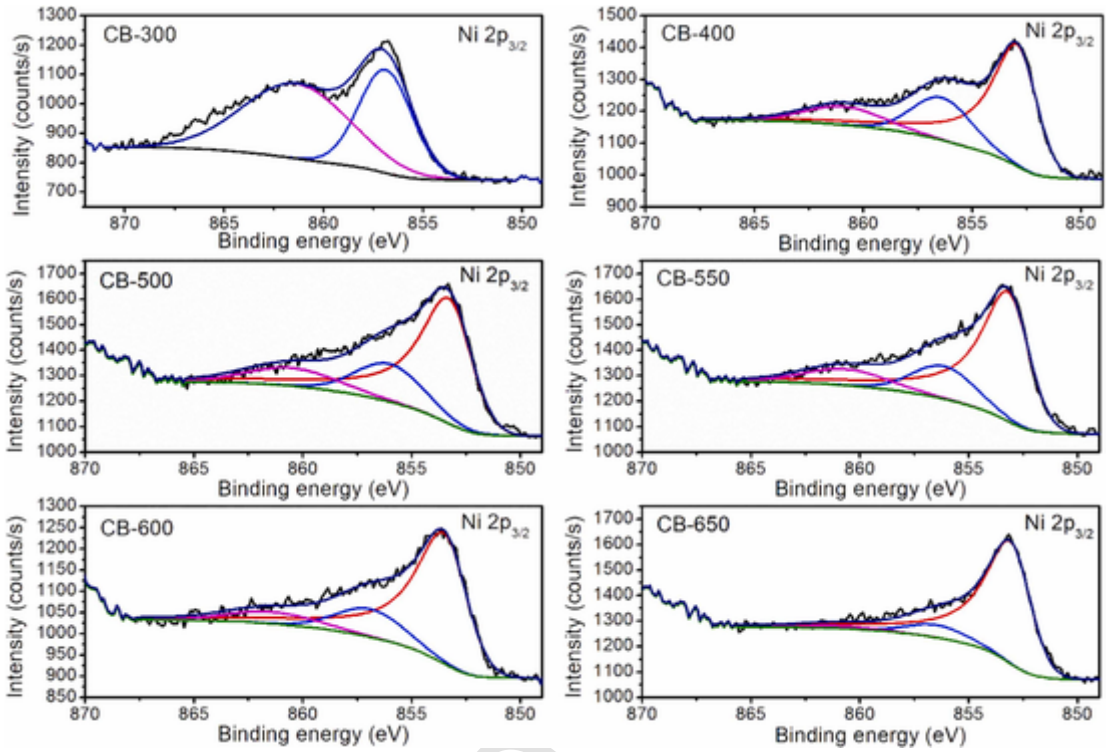

Fig. 5. Fitted Ni 2p $_{3/2}$ XPS spectra of CB-300, CB-400, CB-500, CB-550, CB-600, CB-650 catalysts. Ni (^{0}) = red component, $Ni^{\delta+}$ = blue component, Ni $_{sat.}$ = pink component.

Table 2
Binding energy and contents of Ni^0, $Ni^{\delta+}$ in Ni 2p3/2 level; atomic ratios of Ni and carbon obtained by XPS and corresponding calculated weight ratios.

Catalyst	Ni^o		$N^{\delta+}$		Ni/C	
	B.E. (eV)	at %	B.E. (eV)	at %	at %	wt %
CB-300	–	0	856.9	100	1.26	6.17
CB-400	852.9	55	856.4	45	0.63	3.08
CB-500	853.3	57	856.0	43	0.73	3.57
CB-550	853.2	61	856.1	39	0.67	3.26
CB-600	853.5	66	856.9	33	0.56	2.76
CB-650	853.1	84	856.4	16	0.47	2.32

est amount of surface Ni. But by analysing by ICP, a lowest Ni weight percentage was detected in CB-300. As demonstrated before, there are remaining unreduced reactants in CB-300, which makes Ni dispersed more homogenously than the well reduced Ni particles anchored on the surface of the support after higher temperatures treatments. Thus, the Ni/C ratio of CB-300 (6.17 %) is closer to both the initial value - 10 % and the ratio evaluated by ICP (11.8 %), compared to other samples. And it should be noted that the initial Ni/C ratio engaged in the sol-gel synthesis was calculated to be around 10 %. Once the Ni is well reduced and formed particles with a size larger than 5 nm, not all Ni can be analysed anymore due to the limitation of the XPS detection depth. In addition to the adsorption of carbon on the surface of Ni particles, it leads logically to lower Ni/C surface ratios in CB-400 to CB-650 samples compared to CB-300.

3.2. N_2 physical adsorption properties and H_2 TPD analysis of CB-500, CB-550 and CB-650

The textural properties of CB-500, CB-550 and CB-650 were explored through N_2 adsorption/desorption isotherms as shown in Fig. S3. According to the IUPAC classification [37], Type II isotherms were identified for all the samples, which implies a nonporous or macroporous texture of all the catalysts. The BET surface areas of CB-500, CB-550 and CB-650 are 67, 89, 72 m^2/g, respectively, which is similar to the pure CB support (68 m^2/g). All the BET constant (C) values are around 130, and the differences in surface area values could be due to the experimental errors induced by the weight of samples or by variations in analysis temperature that may be caused by evaporation of liquid N_2. As the catalysts are nonporous and the Ni particles are anchored on the external surface of the support, active sites remain fully accessible to reactants.

Fig. 6 displays H_2 – TPD profiles of CB, CB-500, CB-550 and CB-650 catalysts, that were recorded to estimate the hydrogen uptake and type of adsorption in each case. As shown before, each catalyst has a Ni loading of 19.4 ± 1.3 %. First the samples were reduced and then maintained under H_2 atmosphere until the samples reached the room temperature. After that, Ar was purged to remove the physically-adsorbed H_2. Then H_2 desorption profiles were recorded by heating the sample in the temperature range of 50 – 800 °C and three major desorption peaks were observed with the catalysts samples, while no peak arises with blank CB. A very low temperature desorption peak I observed at around 100 °C could be assigned to the weak type C hydrogen bound to the metal surface in a pre-dissociative form [38]. Another

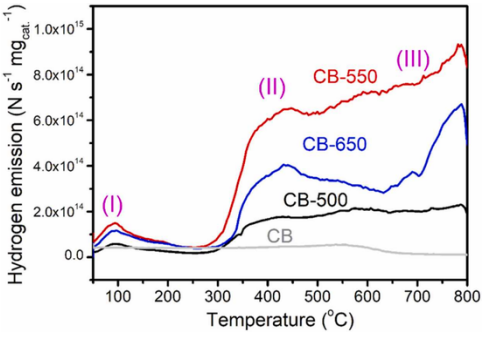

Fig. 6. H_2 TPD profiles of CB blank, CB-500, CB-550, and CB-650 catalysts.

low-temperature peak II at around 400 °C is corresponding to the desorption of the hydrogen atoms bound to the Ni surface in α-state (Ni-H) indicating the exposed portion of Ni atoms [39–43]. The very high H_2 desorption peak III at above 500 °C originated from strongly adsorbing H_2 on corners, edges and high index planes of Ni and spill over hydrogen [38,44]. The intensity of all the peaks vary with respect to the nature of the catalysts. In all cases, the intensity of peaks in CB-550 was the highest, followed by CB-650, then CB-500. Thus, the CB-550 catalyst possesses the highest hydrogen emission value at any temperature compared to the other two, which implies the strongest H_2 adsorption capacity in this sample. The content in Ni^0 and the particle size should be the two main factors determining H_2 adsorption capacity – the higher the Ni^0 content, the smaller the particles, and the more hydrogen uptake. For both factors, CB-550 is listed in the middle of all three samples. Therefore, a proper combination of Ni^0 content and particle size in CB-550 could be the reason for its highest hydrogen uptake. The positions of peak I for all three catalysts exhibit no difference, while the peak II of CB-550 shifted slightly toward lower temperature compared to CB-400 and CB-650, indicating that some weaker hydrogen adsorptions exist in the CB-550 catalyst, which may suggest that more active Ni atoms are present in this catalyst.

3.3. Catalytic performance of CB-400, CB-500, CB-550, CB-600 and CB-650 catalysts

The catalytic performance of Ni supported by CB catalysts with different morphologies were evaluated in the glucose hydrogenation reaction. Since the glucose hydrogenation reaction was carried out in aqueous solution at high temperature and hydrogen pressure, by-products can easily be produced, through for example the isomerization reaction of glucose under water-catalyzed conditions forming mannose and fructose [46], and their reduction product – mannitol, as well as other hydrous thermolysis and dehydration products (Scheme 1) [45]. Therefore, it is necessary to study the yields of by-products to better understand the product selectivity. Fructose, mannose, and mannitol are main by-products analysed here for yield comparison with sorbitol. The conversion of glucose and yields of products are shown in Fig. 7. It is clearly seen that there is a trend of increasing and then decreasing conversion of glucose going from CB-400 to CB-650 catalyst, and the glucose conversion has a maximum value over CB-550 catalyst, which is 33.1 % after 2 h reaction, while the yield of sorbitol has a similar pattern (grey portions). For fructose, the yield has an opposite trend to that of sorbitol, decreasing first and then increasing when the catalyst applied is varied from CB-500 to CB-650. The yield of mannitol (hydrogenation product of fructose) was related to fructose, and when the content of fructose was high, the content of mannitol was also relatively high. The yield of mannose was around 0.8 % for all applied catalysts. Overall, there is a jump in glucose conversion as well as sorbitol yield for the applied catalysts ranging from CB-500 to CB-550, then a large drop from CB-600 to CB-650. This is consistent with the results of sorbitol productivity, namely that sorbitol productivity over CB-550 and CB-600 catalysts showed an absolute superiority compared to other catalysts (Table 3). Turnover frequencies (TOFs) for sorbitol productivity were also calculated to compare the average activity of active sites in each catalyst. Those active sites were determined by H_2 – TPD analysis. Since the hydrogenation of glucose was carried out at 140 °C, the active sites determined by desorbed H_2 from peak I (50–250 °C) in Fig. S4 were taken into account. The calculated TOF values are given in Table 3**.** Those TOFs of 30–56 h^{-1} are in good agreement with the literature values reported for Pt/SBA-15 (45–60 h^{-1}) [9] and for Ni/SiO_2 (7.2–61.2 h^{-1}) [47]. Direct comparison with Ni/CB was not possible as no other contribution uses such formulation for the same reaction, as far as we know. TOFs of CB-550 is slightly higher than CB-500 and CB-650, which indirectly confirms our previous conjecture that more active catalytic sites exist in the CB-550 material.

In order to understand the reasons for the different catalyst performance, first, we plotted the graph of glucose conversion versus Ni average particle size in the different catalysts in Fig. 8a. The glucose conversion increases with the increase of Ni particle size and reaches a maximum at 17.1 ± 6.7 nm, and then it gradually decreases as the size continues to increase. According to our previous work, if the preparation temperature of the Ni/CB catalysts is increased to 750 °C (CB-750), the average particle size of obtained Ni catalysts will rise to 28 nm and the glucose conversion over CB-750 will decrease to 17.6 % [48]., which further indicates that the catalytic performance of Ni/CB decreases with increasing particle size after 17.1 nm. Furthermore, the variation curve of glucose conversion versus metallic Ni content (from XPS) and Ni metal loading (from ICP) is illustrated in Fig. 8b and c. As we have already demonstrated before, metallic Ni is the active phase for the dissociation of hydrogen and substrates adsorption [48]. There, the content of metallic Ni was linearly correlated to the catalytic activity. Therefore, the glucose conversion should maintain its growth from CB-

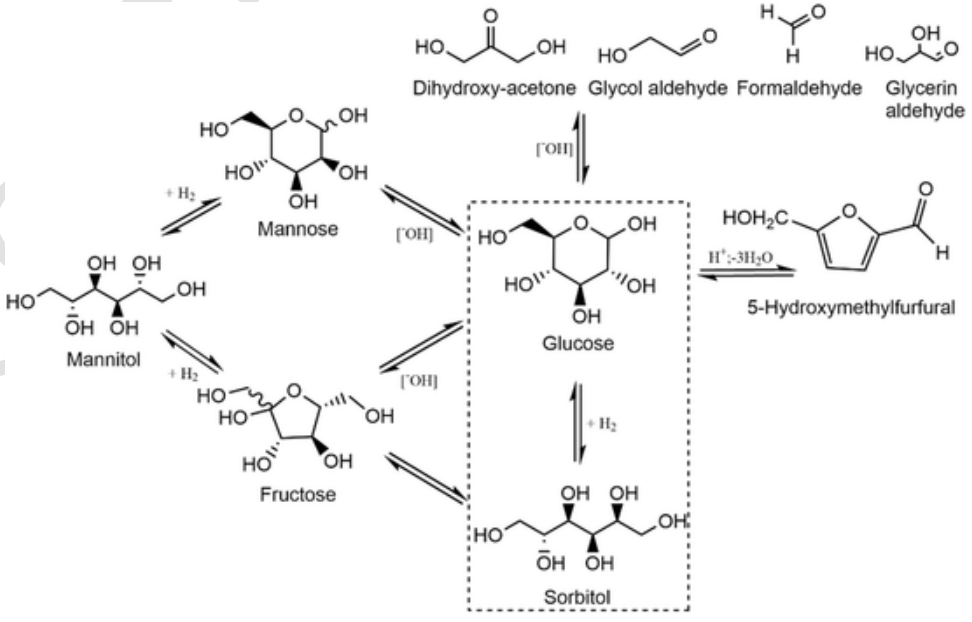

Scheme 1. Reaction network for hydrogenation of glucose [45].

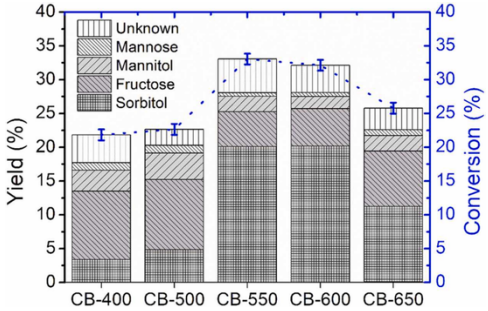

Fig. 7. The conversion of glucose (blue plot) and yields of different products (stack column) under hydrogenation conditions of 140 °C for 2 h and 30 bars of hydrogen with catalysts prepared at various temperatures.

Table 3
Sorbitol productivities with different catalysts calculated by using Equation 6 and sorbitol turnover frequencies (TOFs) calculated from H_2 – TPD curves (peak I). Reaction condition: 60 mg of catalysts, 0.5 g of glucose, 140 °C, 30 bar of hydrogen, 2 h.

Catalyst	Glucose conversion / %	Sorbitol / mg	Productivity / $kg.g_{cat.}^{-1}.min^{-1}$	TOF (sorbitol production) / h^{-1}
CB-400	21.8	17.6	2.4	–
CB-500	22.7	24.9	3.5	30
CB-550	33.1	104.5	14.5	56
CB-600	32.1	103.9	14.4	–
CB-650	25.8	57.6	8	44

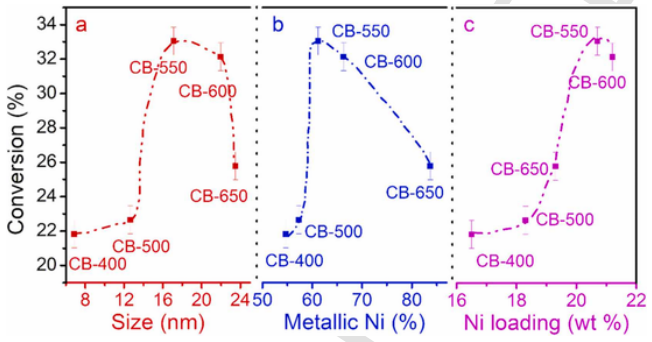

Fig. 8. Glucose conversion vs Ni particle size in the applied catalysts (a), and vs metallic Ni content determined by XPS (b), and Ni metal loading analysed by ICP in the applied catalysts (c). The dash-dot lines connecting the points in the graphs are hand-drawn to highlight the trends.

400 to CB-650 due to the increase in metallic Ni content among the catalysts, but here it is not the case. In Fig. 8b, the glucose conversion increases accordingly before the CB-550 catalyst, but after that, this conversion decreases. Thus, here the surface metallic Ni is not the dominant factor for obtaining a high glucose conversion after CB-550. By analysing the Ni loading vs glucose conversion among CB-400, CB-500 and CB-550 (Fig. 8c), we found that glucose conversion increased with Ni loading in the catalysts. The Ni loading in CB-550, CB-600 and CB-650 catalysts are similar, but the glucose conversions show a distinguish difference. Herein, a crucial factor – particle size must play a key role in governing the activity of the catalysts, which will be elaborated further below.

Similarly, by graphing sorbitol selectivity versus size as well as versus the content of metallic Ni, a similar conclusion as the conversion was reached, that is, the sorbitol product selectivity shows a trend of increasing and then decreasing with increasing size and has a maximum at 17.1 nm. It also shows that sorbitol selectivity rises and then falls with the increase in metallic Ni content (Fig. S5). The higher H_2 adsorption ability of the CB-550 catalyst highlighted by H_2 – TPD analysis enhances the hydrogenation activity compared to CB-650 and CB-500 catalysts, which has been testified by other authors comparing Co-B and Ni-B catalysts where best performance resulted from the strong hydrogen adsorption ability on the catalyst surface [5].

3.4. Catalytic performance of GNP-450, GNP-550, and GNP-650

The synthesis method of Ni/CB catalysts was applied for the preparation of graphene nanoplatelets catalysts, named GNP-450, GNP-550 and GNP-650 as function of the heat-treatment applied. The p-XRD patterns of prepared catalysts as well as of the pure GNP support are shown in Fig. S6. The diffraction peaks assigned to Ni (111) and Ni (200) at $2\theta = 44.5°$ and 51.8° show a similar change as in the Ni/CB series catalysts, which corresponds to the fact that the size of Ni particles increase with increasing reduction temperature on the GNP carrier. Unlike CB support, GNP displays an intense diffraction peak at $2\theta = 26.5°$, which is corresponding to the characteristic crystalline graphite (002) plane [49]. The grain size of Ni particles over GNP support was also calculated using the Scherrer equation and the result is shown in Table S1. The average grain sizes of GNP-450, GNP-550 and GNP-650 were 7.5, 16.6 and 20.6 nm, respectively. TGA profiles of GNP series catalysts (Fig. S7) indicate that the GNP-450 catalyst possesses an incompletely decomposed reactant mixture from the preparation process, which is similar to the result with CB-400 catalyst. N_2 sorption isotherms (Type IV) of GNP-450, GNP-550 and GNP-650 samples (Fig. S8) indicate a mesoporous texture and the type H4 loops are associated with narrow slit pores [37]. The BET specific areas exhibit similar values around 90 m^2g^{-1}(Table S1). Bulk and surface Ni percentages in GNP catalysts were verified using ICP-AES and XPS elemental analysis (Table S1), which testifies that GNP-450, GNP-550 and GNP-650 catalysts have similar Ni contents. XPS was also applied to analyse the metallic Ni contents on the surface of GNP samples, the results are shown in Table S1. GNP-450 and GNP-550 have a similar Ni^0 content, around 30 %, and both are higher than in GNP-650.

As with the CB series catalysts, the glucose hydrogenation reaction was used to verify the catalytic performance of GNP-450, GNP-550 and GNP-650 catalysts. The glucose conversion after 2 h reaction over those three catalysts is illustrated in Fig. S9. The conversion shows the same pattern as before with CB series catalysts, appearing to increase and then decrease as the catalysts change from GNP-450 to GNP-650. The highest glucose conversion was observed over GNP-550 with an average Ni grain size around 16.6 nm, which is similar to the nanoparticle size of CB-550 catalysts. However, the glucose conversion over GNP-550 catalyst (20.9 %) is not as high as that over CB-550 (33.1 %), which may be due to the lower content of Ni^0 in GNP-550 catalyst or to the different interactions between Ni particles and CB/GNP supports. This lower content of Ni^0 in GNP-550 can be further testified by the lower atomic Ni/O ratio (0.26) by comparison with CB-550 catalyst (0.35) calculated by XPS.

In general, supported Ni catalysts prepared at 550 °C with an average size around 16 nm show the highest catalytic performance regardless of whether CB or GNP supports were used, and catalysts obtained with CB support has a higher catalytic performance than those using GNP support. Similar results were observed in the CO_2 methanation reaction over Ni/YSZ catalysts. Ni particle size with 19 nm has a good performance due to the high Ni^0 dispersion [50]. And Ni nanoparticles in the size range of 10–20 nm were also exhibiting the best catalytic performance for CO methanation reaction compared to smaller (5–10 nm) and bigger (20–35 nm) particle range, because carbon deposits easily onto small Ni particles and carbon nanofibers can grow fast onto big particles [51]. Besides, small particles with more edges and

corners favour the adsorption of one reactant versus the other, resulting in less reaction possibilities compared to medium size particles. For instance, based on DFT calculations, stepped surfaces of Au particles with more edges atoms were shown to be preferentially chemisorbed with substrates like CO, O and O_2 [52]. By opposition, big particles certainly lose the active metal surface (number of adsorption sites) compared to medium ones. Thus, particles with a medium size can achieve highest activity, as exemplified also with 7 nm nanoparticles in glucose oxidation with a good compromise balance of adsorption of the reactants [25]. In summary, the metallic phase on the catalyst surface is generally a positive correlation for the hydrogenation reaction. Indeed, for all catalysts treated up to 550 °C, there is an increase in catalytic performance with the increase in metallic phase content, but after that temperature, this correlation does not exist anymore. Since the particles were grown due to the sintering, larger grain sizes were obtained. In that case, less atoms are present in low-coordination (LC) sites that are considered to have enhanced reactivity (edge/corner sites). In other words, CB-550 contains more LC Ni atoms that CB-650, so its activity is higher. This also corresponds to the calculated TOFs – TOF of CB-550 is higher than that of CB-650. In addition, small particles certainly possess more metal surface area than big ones, which also was reflected in H_2 – TPD results. By opposition, since the smallest size of our Ni particles is 7 nm, this size is too large to take the small size effect on the surface electronic structure into account. Thus, CB-550/GNP-550 is the best compromise presenting small Ni nanoparticles with more LC sites, high metal surface area and high metallic phase, and its average particle size is 17 nm.

3.5. Stability of catalysts

A recycling test of CB-550 catalyst was performed to study its stability, and glucose conversion and product yields over fresh and spent catalysts are compared in the figure below. In Fig. 9, it can be seen that glucose conversion and sorbitol yield dropped from 33.1 % to 29.6 % and from 20.1 % to 15.8 %, respectively, implying some deactivation of the Ni catalysts during use, which is consistent with our previous work [48]. By comparing the yields of different products in the recycling use, we found sorbitol still remained the dominant product, and the yields of fructose and mannitol slightly increased, which may be due to the fact that the catalyst lost some active sites for hydrogenation but potentially created new active sites (like $Ni^{\delta+}$) catalysing glucose isomerization.

In order to find out the reasons for catalyst deactivation, AAS analysis was applied on the filtrate to reveal if Ni leaching occurred during glucose hydrogenation. After two hours, 5.4 ppm of Ni was detected in the aqueous solution, which is around 4.3 % of Ni leached from the catalyst, as calculated by the equation below:

$$\text{Nileachingpercentage} = \frac{C_{\text{leached}} \times V_{\text{solution}}}{m_{\text{initial}}} \times 100$$

where C_{leached} is the concentration of leached Ni species detected by AAS, V_{solution} represents the volume of reaction medium, and m_{initial} is the total weight of Ni in the fresh catalyst.

This Ni leaching was also reflected in the decrease of grain size of Ni particles. Fig. 10 shows the XRD patterns of CB-550 catalyst before (Fresh) and after (Spent) catalytic reaction. Based on the FWHM of Ni (111) at 2θ value around 44.51°, Debye–Scherrer formula was applied to calculate the average grain size of Ni particles. A size decrease of Ni particles from 19.1 to 17.7 nm was uncovered. Thus, a leaching inducing some catalyst deactivation was detected during hydrogenation reaction, which is normally inevitable for Ni based catalysts in aqueous solution under harsh reaction conditions [19]. Work will be carried out in the future on the real time monitoring of leaching to find out the mechanism and mitigate it by changing the reaction conditions.

4. Conclusions

In situ XRD was used to study Ni particle growth on a Carbon Black (CB) support with temperature, and it was found that the growth of particles is more obvious in the temperature range of 450–550 °C compared to other temperatures. Thus, CB-400, CB-500, CB-550, CB-600 and CB-650 catalysts were chosen to be prepared at the corresponding temperatures, whose Ni particle size were analysed to be 6.9 ± 1.3, 12.6 ± 3.8, 17.1 ± 6.7, 22.0 ± 10.0 and 23.5 ± 11.6 nm respectively, by the statistical analysis of particles in TEM images. TGA analysis indicated the presence of undecomposed portion of reaction mixture in the CB-400 catalyst. The relative contents of Ni and C on the catalyst surface obtained by XPS analysis were all in the 2.32 – 3.04 range, while the content in metallic Ni increases from CB-400 catalyst (55 %) to CB-650 catalyst (84 %). H_2 desorption analysis highlighted that CB-550 exhibits the highest hydrogen uptake and the weakest adsorbed hydrogen, compared to CB-450 and CB-650. Furthermore, the glucose hydrogenation reaction with CB-550 catalyst was found to have the highest glucose conversion (33.1 %) and sorbitol selectivity (62.8 %) within 2 h compared to other catalysts, which can be explained by a combined effect of high metallic phase content, more LC sites and high metal surface area. The same conclusion was reached by replacing CB support with GNP support: GNP-550 has the best catalytic performance relative to GNP-450 and GNP-650, but GNP-550 is not superior to CB-550 catalyst, highlighting a support effect. Besides, limited Ni leaching was uncovered during hydrogenation reaction leading to some deactivation of the catalyst, that could be mitigated by optimization work carried out in the future. The preparation of Ni catalysts presenting different particle sizes by simple control of the temperature of the synthesis condi-

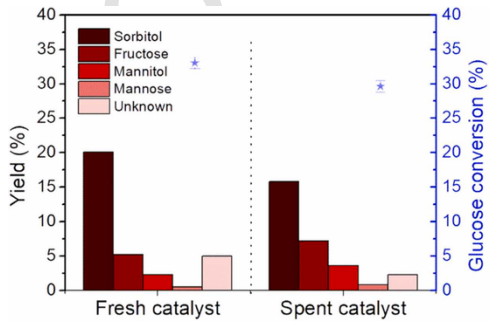

Fig. 9. Glucose conversions (blue stars) and product yields (red columns) over fresh and spent CB-550 catalyst. Reaction conditions: 60 mg catalyst, 0.5 g glucose, 100 mL H_2O, T = 120 °C, p (H2) = 30 bar, 120 min and stirring speed of 1700 rpm.

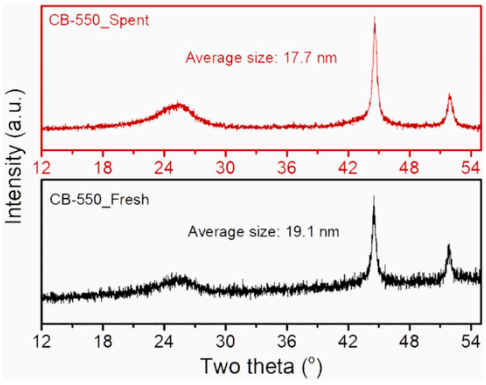

Fig. 10. Powder X-ray diffraction patterns of CB-550_Fresh (black) and CB-550_Spent (red) catalysts.

tions to alter their catalytic performance was achieved in this work and size effect was demonstrated to exist in nanoparticles larger than 10 nm, which could bring a reference for the development of non-precious metal catalysts for biomass conversion.

CRediT authorship Contribution statement

Yang Fu: Conceptualization, Formal analysis, Investigation, Methodology, Validation, Visualization, Writing – original draft; **François Devred:** Investigation, Validation; **Pierre Eloy:** Investigation, Validation; **Tommy Haynes:** Investigation; **Michael L. Singleton:** Supervision, Writing – review & editing; **Sophie Hermans:** Conceptualization, Funding acquisition, Project administration, Resources, Supervision, Validation, Writing – review & editing.

Declaration of Competing Interest

The authors declare that they have no known competing financial interests or personal relationships that could have appeared to influence the work reported in this paper.

Data Availability

Data will be made available on request.

Acknowledgements

The authors gratefully acknowledge Jean-François Statsyns for technical assistance, IMERYS GRAPHITE & CARBON (Switzerland) firm for generous donation of carbon black. Y. F. thanks China Scholarship Council (CSC) for the financial support.

Conflicts of interest

There are no conflicts to declare.

Appendix A. Supporting information

Supplementary data associated with this article can be found in the online version at doi:10.1016/j.apcata.2022.118833.

References

[1] Sorbitol Market Size, Share and Global Trend By Type, Application, and Geography Forecast 2019–2026, Sorbitol Market, Fortune Business Insights, 2019, pp. 135.
[2] P. Gallezot, P.J. Cerino, B. Blanc, G. Flèche, P. Fuertes, J. Catal. 146 (1994) 93–102, https://doi.org/10.1016/0021-9517(94)90012-4.
[3] L. Hui, L. Hexing, W. Weijiang, D. Jing-Fa, Chem. Lett. 28 (1999) 629–630, https://doi.org/10.1246/cl.1999.629.
[4] H. Li, W. Wang, J. Fa Deng, J. Catal. 191 (2000) 257–260, https://doi.org/10.1006/jcat.1999.2792.
[5] H. Li, H. Li, M. Wang, Appl. Catal. A: Gen. 207 (2001) 129–137, https://doi.org/10.1016/S0926-860X(00)00662-1.
[6] H. Li, H. Li, J.F. Deng, Catal. Today 74 (2002) 53–63, https://doi.org/10.1016/S0920-5861(01)00530-2.
[7] D.K. Mishra, J.M. Lee, J.S. Chang, J.S. Hwang, Catal. Today 185 (2012) 104–108, https://doi.org/10.1016/j.cattod.2011.11.020.
[8] J. Zhang, S. Wu, Y. Liu, B. Li, Catal. Commun. 35 (2013) 23–26, https://doi.org/10.1016/j.catcom.2013.01.017.
[9] X. Zhang, L.J. Durndell, M.A. Isaacs, C.M.A. Parlett, A.F. Lee, K. Wilson, ACS Catal. 6 (2016) 7409–7417, https://doi.org/10.1021/acscatal.6b02369.
[10] L.M. Sanz-Moral, A. Aho, N. Kumar, K. Eränen, M. Peurla, J. Peltonen, D.Y. Murzin, T. Salmi, Catal. Lett. 148 (2018) 3514–3523, https://doi.org/10.1007/s10562-018-2556-4.
[11] H. Singh, A. Rai, R. Yadav, A.K. Sinha, Mol. Catal. 451 (2018) 186–191, https://doi.org/10.1016/j.mcat.2018.01.010.
[12] B. Zada, L. Yan, Y. Fu, Sci. China.: Chem. 61 (2018) 1167–1174, https://doi.org/10.1007/s11426-018-9321-0.
[13] M.Y. Byun, D.-W. Park, M.S. Lee, Catal. Today 352 (2019) 88–94, https://doi.org/10.1016/j.cattod.2019.12.039.
[14] P.M. de Souza, L. Silvester, A.G.M. da Silva, C.G. Fernandes, T.S. Rodrigues, S. Paul, P.H.C. Camargo, R. Wojcieszak, Catalysts 9 (2019) 132, https://doi.org/10.3390/catal9020132.
[15] S. Esposito, B. Silvestri, V. Russo, B. Bonelli, M. Manzoli, F.A. Deorsola, A. Vergara, A. Aronne, M. Di Serio, ACS Catal. 9 (2019) 3426–3436, https://doi.org/10.1021/acscatal.8b04710.
[16] J. So, Y. Chung, D.S. Sholl, C. Sievers, Mol. Catal. 475 (2019) 110423, https://doi.org/10.1016/j.mcat.2019.110423.
[17] S. Carlier, J. Gripekoven, M. Philippo, S. Hermans, Appl. Catal., B 282 (2021) 119515, https://doi.org/10.1016/j.apcatb.2020.119515.
[18] V.J. Ipatieff, Ber. dtsh. Chem. Ges. (1912) 3218.
[19] B. Kusserow, S. Schimpf, P. Claus, Adv. Synth. Catal. 345 (2003) 289–299.
[20] M. Haruta, Catal. Today 36 (1997) 153–166, https://doi.org/10.1016/S0920-5861(96)00208-8.
[21] B.R. Cuenya, S.-H. Baeck, T.F. Jaramillo, E.W. McFarland, J. Am. Chem. Soc. 125 (2003) 12928–12934, https://doi.org/10.1021/ja036468u.
[22] S.K. Shaikhutdinov, R. Meyer, M. Naschitzki, M. Bäumer, H.J. Freund, Catal. Lett. 86 (2003) 211–219, https://doi.org/10.1023/A:1022616102162.
[23] T. Ishida, N. Kinoshita, H. Okatsu, T. Akita, T. Takei, M. Haruta, Angew. Chem. - Int. Ed. 47 (2008) 9265–9268, https://doi.org/10.1002/anie.200802845.
[24] M. Haruta, S. Tsubota, T. Kobayashi, H. Kageyama, M.J. Genet, B. Delmon, J. Catal. 144 (1993) 175–192, https://doi.org/10.1006/jcat.1993.1322.
[25] T. Haynes, V. Dubois, S. Hermans, Appl. Catal. A: Gen. 542 (2017) 47–54, https://doi.org/10.1016/j.apcata.2017.05.008.
[26] N. Meyer, D. Pirson, M. Devillers, S. Hermans, Appl. Catal. A: Gen. 467 (2013) 463–473, https://doi.org/10.1016/j.apcata.2013.07.045.
[27] Y. Lykhach, S.M. Kozlov, T. Skála, A. Tovt, V. Stetsovych, N. Tsud, F. Dvořák, V. Johánek, A. Neitzel, J. Mysliveček, S. Fabris, V. Matolín, K.M. Neyman, J. Libuda, Nat. Mater. 15 (2016) 284–288, https://doi.org/10.1038/nmat4500.
[28] G.L. Bezemer, J.H. Bitter, H.P.C.E. Kuipers, H. Oosterbeek, J.E. Holewijn, X. Xu, F. Kapteijn, A.J. van Dillen, K.P. de Jong, J. Am. Chem. Soc. 128 (2006) 3956–3964, https://doi.org/10.1021/ja058282w.
[29] F. Mederos-Henry, J. Mahin, B.P. Pichon, M.M. Dîrtu, Y. Garcia, A. Delcorte, C. Bailly, I. Huynen, S. Hermans, Nanomaterials 9 (2019) 1196, https://doi.org/10.3390/nano9091196.
[30] J.M. Ting, R.Y. Lin, J. Mater. Sci. 30 (1995) 2382–2389, https://doi.org/10.1007/BF01184590.
[31] C. Su, B.Y. Hong, C.M. Tseng, Catal. Today 96 (2004) 119–126, https://doi.org/10.1016/j.cattod.2004.06.132.
[32] K.E.J. Lehtinen, M.R. Zachariah, J. Aerosol Sci. 33 (2002) 357–368, https://doi.org/10.1016/S0021-8502(01)00177-X.
[33] T.W. Hansen, A.T. DeLaRiva, S.R. Challa, A.K. Datye, Acc. Chem. Res. 46 (2013) 1720–1730, https://doi.org/10.1021/ar3002427.
[34] C. Vriamont, T. Haynes, E. McCague-Murphy, F. Pennetreau, O. Riant, S. Hermans, J. Catal. 329 (2015) 389–400, https://doi.org/10.1016/j.jcat.2015.06.003.
[35] C.F. Holder, R.E. Schaak, ACS Nano 13 (2019) 7359–7365, https://doi.org/10.1021/acsnano.9b05157.
[36] M.C. Biesinger, B.P. Payne, A.P. Grosvenor, L.W.M. Lau, A.R. Gerson, R.S.C. Smart, Appl. Surf. Sci. 257 (2011) 2717–2730, https://doi.org/10.1016/j.apsusc.2010.10.051.
[37] K.S.W. Sing, Pure Appl. Chem. 57 (1985) 603–619, https://doi.org/10.1351/pac198557040603.
[38] J.A. Konvalinka, P.H. Van Oeffelt, J.J.F. Scholten, Appl. Catal. 1 (1981) 141–158, https://doi.org/10.1016/0166-9834(81)80002-4.
[39] K. Christmann, O. Schober, G. Ertl, M. Neumann, J. Chem. Phys. 60 (1974) 4528–4540, https://doi.org/10.1063/1.1680935.
[40] A.G. Boudjahem, S. Monteverdi, M. Mercy, M.M. Bettahar, J. Catal. 221 (2004) 325–334, https://doi.org/10.1016/j.jcat.2003.08.002.
[41] Y. Cesteros, P. Salagre, F. Medina, J.E. Sueiras, Appl. Catal. B: Environ. 25 (2000) 213–227, https://doi.org/10.1016/S0926-3373(99)00133-2.
[42] A.-G. Boudjahem, S. Monteverdi, M. Mercy, M.M. Bettahar, Catal. Lett. 97 (2004) 177–183, https://doi.org/10.1023/B:CATL.0000038581.80872.7b.
[43] S. Dekura, H. Kobayashi, R. Ikeda, M. Maesato, H. Yoshino, M. Ohba, T. Ishimoto, S. Kawaguchi, Y. Kubota, S. Yoshioka, S. Matsumura, T. Sugiyama, H. Kitagawa, Angew. Chem. Int. Ed. 57 (2018) 9823–9827, https://doi.org/10.1002/anie.201805753.
[44] S. Velu, S.K. Gangwal, Solid State Ion. 177 (2006) 803–811, https://doi.org/10.1016/j.ssi.2006.01.031.
[45] B. Kusserow, S. Schimpf, P. Claus, Adv. Synth. Catal. 345 (2003) 289–299, https://doi.org/10.1002/adsc.200390024.
[46] J.M. Los, L.B. Simpson, K. Wiesner, J. Am. Chem. Soc. 78 (1956) 1564–1568, https://doi.org/10.1021/ja01589a017.
[47] S. Schimpf, C. Louis, P. Claus, Appl. Catal. A: Gen. 318 (2007) 45–53, https://doi.org/10.1016/j.apcata.2006.10.034.
[48] Y. Fu, L. Ding, M.L. Singleton, H. Idrissi, S. Hermans, Appl. Catal. B: Environ. 288 (2021) 119997, https://doi.org/10.1016/j.apcatb.2021.119997.
[49] Z.Q. Li, C.J. Lu, Z.P. Xia, Y. Zhou, Z. Luo, Carbon 45 (2007) 1686–1695, https://doi.org/10.1016/j.carbon.2007.03.038.
[50] J.K. Kesavan, I. Luisetto, S. Tuti, C. Meneghini, G. Iucci, C. Battocchio, S. Mobilio, S. Casciardi, R. Sisto, J. CO2 Util. 23 (2018) 200–211, https://doi.org/10.1016/j.jcou.2017.11.015.
[51] J. Gao, C. Jia, M. Zhang, F. Gu, G. Xu, F. Su, Catal. Sci. Technol. 3 (2013) 2009–2015, https://doi.org/10.1039/C3CY00139C.
[52] M. Mavrikakis, P. Stoltze, J.K. Nørskov, Catal. Lett. 64 (2000) 101–106, https://doi.org/10.1023/A:1019028229377.